

Simone Cannarozzo

Isomeric yield ratio studies in nuclear reactions and alpha-particle induced fission of Thorium

Licentiate thesis



UPPSALA
UNIVERSITET

Abstract

Despite decades of research since the initial discovery of nuclear fission, numerous unresolved questions still persist. It is known empirically that fission fragments emerge with high angular momentum. The mechanism responsible for the generation of the large angular momenta observed is one of these open questions. Since the characteristics of fission fragments are not directly measurable, experimentally accessible observables are used to derive the angular momenta using nuclear model codes. One of these observables is the yield ratio between fission products produced in different isomeric states, *i.e.*, metastable energy levels of the same nucleus.

In this thesis, a study of the level density models implemented in the nuclear model code TALYS is presented. Simulated and experimental isomeric yield ratios of a large number of nuclear reactions is compared. The results show a bias in the models that favours the population of the high-spin states and that this can be produced by the overestimation of the spin width distribution. The reason for this study is to improve the models then used in the angular momentum calculation.

Moreover, the isomeric yield ratio measurement of twenty-one FFs is presented. The measurement was performed using the JYFLTRAP system at the University of Jyväskylä. The fission fragments were produced by the 32 MeV alpha-particle induced fission of ^{232}Th . The analysis process, involving different identification and correction methods, and preliminary results are presented.

List of papers

This thesis is based on the following papers, which are referred to in the text by their Roman numerals.

- I Cannarozzo, S., Pomp, S., Solders, A. et al. Global comparison between experimentally measured isomeric yield ratios and nuclear model calculations. Eur. Phys. J. A 59, 295 (2023).
<https://doi.org/10.1140/epja/s10050-023-01202-5>
My contribution: I wrote most of the manuscript and developed the codes to process EXFOR data, ran the TALYS calculations and analyzed the results.

Reprints were made with permission from the publishers.

Contents

1	Introduction	7
1.1	Brief introduction of the fission process	7
1.2	Angular momentum of fission fragments	8
1.3	From excited fission fragments to isomers	9
2	Global study of IYR in reactions	11
2.1	Introduction	11
2.2	Experimental data	12
2.3	TALYS models and calculations	13
2.4	Comparison between experimental and calculated data	14
2.5	Results and discussion	16
3	Isomeric yield ratio measurement	18
3.1	Introduction	18
3.2	Experimental setup	21
3.2.1	IGISOL	21
3.2.2	Ions motion in Penning traps	22
3.2.3	Bunch cleaning: side-band cooling technique	22
3.2.4	Precision trap: PI-ICR	23
3.2.5	PI-ICR for IYR measurements	25
3.3	Identification methods	26
3.3.1	Angular cut	27
3.3.2	Angular cut with fitted sigma	27
3.3.3	Clustering: OPTICS	28
3.3.4	Comparison between identification methods	29
3.4	Corrections	30
3.4.1	Decay correction	31
3.4.2	MCP efficiency correction	33
3.4.3	Effect of the corrections	34
3.5	Results and discussion	34
4	Conclusions and future outlook	36
	References	38

1. Introduction

Despite decades of research since the initial discovery of nuclear fission nearly a century ago [1], numerous unresolved questions still persist in our understanding of this physical process. Nuclei are very complex systems, characterized by a variable number of nucleons (neutrons and protons) interacting through strong and electromagnetic interactions. The solution to this many-body problem to achieve a microscopic description of the nuclear dynamical evolution is extremely complex. This makes fission a very challenging reaction to describe.

1.1 Brief introduction of the fission process

Fission is driven by a reduction of the potential energy of the system, that can, spontaneously or under the action of an incident particle, start a series of events that end up in two (or more) stable (or metastable) nuclei [2]. A wide variety of models have been developed over the years to interpret the many empirical observations.

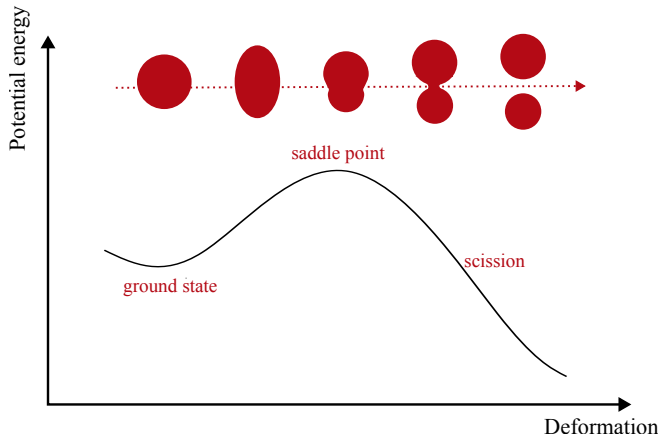


Figure 1.1. Potential energy evolution with respect to deformation for a fissioning system described by the liquid drop model.

A simple but effective model to describe the evolution of fission is the liquid drop model (LDM) first advanced by G. Gamow in 1935 [3]. This model is far too simple to correctly describe many observations, but is sufficient to

show, in principle, how fission advances. According to the LDM, the nucleus behaves like a drop of an incompressible fluid whose stability depends on the equilibrium between cohesive nuclear forces and repulsive Coulomb interactions. Two more factors have been added to account for the higher stability of nuclei with the same number of protons and neutrons, especially for lower masses, and with even numbers of nucleons.

The fissioning nucleus can then be seen as a drop which evolves as shown in Figure 1.1. When the fission process starts, the nucleus progressively deforms until it reaches the so-called saddle point, where the evolution toward two separated nuclei can not be reversed anymore. Here the two nuclei that started forming are pushed apart by the Coulomb repulsion overcoming the cohesive forces and a neck connecting the two nuclei forms. This neck eventually, at scission, breaks and the two FFs are produced. Both these points are conventionally defined and do not correspond to a specific arrangement of nucleons.

1.2 Angular momentum of fission fragments

It is known empirically that fragments emerge from fission spinning at high energy. It has been demonstrated that FFs are produced with high angular momenta (from few to around $10\hbar$), even when the fissioning nucleus has zero initial momentum [4]. The generation of this angular momentum is still an open and debated question: several competing models have indeed been advanced to explain it [5, 6, 7, 8, 9, 10]. They can generally be divided into pre- and post-scission models, referring to whether the angular momentum is generated before or after the neck rupture.

In pre-scission models, the nucleus is generally seen, between the saddle and scission points, as a superposition of two nascent fragments moving with respect to each other. The collective rotations of the nascent fragments would be responsible for the angular momentum generation, which would preserve memory of the initial system. In post-scission models the angular momentum arises from the interaction of the two fragments after scission, *e.g.*, by Coulomb interaction.

The recent model by Wilson *et al.* [6] advanced the idea of a post-scission generation mechanism that leads to FFs with completely uncorrelated spins. The angular momentum is, from a classical point of view, compared to the torque generated by the rupture of the neck connecting the two FFs.

Even though angular momenta can not be directly measured, as the prompt neutrons emission proceeds too rapidly, data are needed in order to test the predictions of different models. Therefore, observations on the products of the de-excitation process of fission fragments are needed, in order to derive their angular momenta.

1.3 From excited fission fragments to isomers

After scission, the highly excited FFs can de-excite by emitting neutrons and γ -rays. As long as the excitation energy is larger than the neutron separation energy (S_n), nuclei can emit the so-called prompt neutrons to de-excite. At lower excitation energies, when the neutron emission is energetically unlikely, the FFs are conventionally called secondary fission fragments or fission products (FPs). At this stage, the FPs de-excite emitting prompt statistical and then discrete γ -rays until they reach either the ground state or a long lived excited state. Such states are called isomers and can have half-lives ranging from several ns to 10^{15} years like, *e.g.*, ^{180m}Ta .

Although three kinds of isomers exist (spin-traps, K-traps and shape isomers), this work is focused on spin traps, *i.e.*, isomers whose decay to lower energy levels is retarded by a large difference in nuclear spin and the unlikelihood of emitting radiation to meet this variation [11]. These kind of isomers can usually be found close to magic numbers, corresponding to closed neutron and proton shells thus mainly around mass numbers 90, 130, 150 and 210.

The fraction of nuclei decaying into the two states is called isomeric yield ratio (IYR) and, in this work, it is defined as:

$$IYR = \frac{Y_{hs}}{Y_{hs} + Y_{ls}} \quad (1.1)$$

Where Y_{hs} and Y_{ls} are the yields corresponding to, respectively, the high- and low-spin states.

As a result of the de-excitation process explained so far, the IYR depends on the initial excitation energy and angular momentum of the fission fragments [12]. The IYR can be experimentally measured using different techniques, *e.g.*, γ -spectroscopy and the phase-imaging ion-cyclotron-resonance [13, 14].

The IYR can then be used to calculate the angular momentum of the FFs: the de-excitation process of FFs to the metastable state is described by several models that can also be used to deduce the angular momentum starting from the IYR. This is done by simulating the de-excitation process for several initial excitation conditions, until the computed IYR resulting from this calculations matches the experimentally measured one [13, 15, 16, 17]. This makes the IYR a suitable fission observable to deduce the angular momentum of FFs and motivates the efforts to measure it for different fragments and fissioning nuclei.

The work described here concerns two parts of this process. The first part (Chapter 2) is focused on testing the nuclear model codes used for the de-excitation calculations comparing their results to experimentally measured IYRs of reaction products.

In the second part (Chapter 3), the IYR measurement campaign of $\text{Th}(\alpha, f)$ fission products is presented. This is the first measurement of the IYRs of this fissioning system, which was chosen to study the effect of the angular

momentum added to the system by the projectile α particles on the ratios and on the angular momentum of fission fragments.

2. Global study of IYR in reactions

2.1 Introduction

The goal of the first part of this work is to study the reliability of the models used in the angular momentum calculations and it is presented in Paper I [18]. To do so, data for a large number of reactions were retrieved from the EXFOR nuclear data library [19] and it was tried to reproduce them using the TALYS nuclear model code [20, 21]. TALYS is an open-source nuclear reaction program which can be used to calculate many nuclear reaction data and information, such as cross sections, γ -ray and neutron multiplicities and IYRs. It is a widely used software for the analysis and prediction of nuclear reactions involving photons and light particle projectiles (neutrons, protons, deuterons, ^3He , and α particles) and nearly all the nuclides of the nuclear chart in the energy range 0-200 MeV.

Thanks to the possibility to tune the parameters of the calculations in order to match the experimental results, it is a powerful tool to analyse and test the theoretical models implemented with respect to empirical data. This is what has been done in this work with the models for the density of the nuclear energy levels in the continuum region.

To calculate the IYR of a nucleus resulting from a reaction, mainly two steps are involved: the calculation of the initial status of the de-exciting nucleus and the following de-excitation. Several models are implemented for the first stage, depending on the particles and energies involved, *i.e.*, the so-called optical model to describe compound reactions or the γ -ray strength functions for reactions involving absorption and emission of photons. These models have largely been tested by the TALYS community, being the main elements of, *e.g.*, cross section calculations [20].

The second stage is governed by the models that calculate, in the continuum energy region, the density of nuclear states as a function of energy and spin. Nuclei have several states (levels) defined by their energy, spin and parity and, typically, the higher the energy, the denser are the levels. Above few MeV, the spacing between levels reduces to a point where a discrete description is not possible anymore and is, instead, replaced by a statistical continuous description. Several models have been developed to calculate the level density, defined as the number of nuclear levels around an excitation energy for a set spin and parity. These models are called level density models (LDM) and they are one of the main ingredients of the calculation of the population of spin isomers. Moreover, while the specific model used to calculate the entrance

Table 2.1. *Composition of the database divided into the six considered projectile particles, showing both the number of entries and experimental data.[18]*

Projectile	Entries	Experimental points
n	498	1382
γ	290	1245
α	151	1243
p	138	999
^2H	40	334
^3He	13	156
Total	1130	5359

channel depends on the reaction involved, the LDMs are always used to define the density of the energy levels of the de-exciting nuclei.

The dependence of the IYR on the width of the distribution of energy levels with respect to the spin was investigated with TALYS by modifying the parameter that controls this width, *i.e.*, the so-called spin cut-off parameter. In paper I it is shown that a lower spin cut-off parameter, corresponding to narrower spin distributions, yields, on average, results closer to the experimental IYRs. In particular, such a reduction limits a bias according to which the models implemented in TALYS favor the high-spin state in the isomeric pair.

2.2 Experimental data

The total experimentally measured IYRs retrieved from the EXFOR library for this work are 5.359. They are collected in 1.131 entries, *i.e.*, single experiments in one or more bibliographic references. Entries are the basic elements of the library and can contain more than one IYR, differing by just the energy of the incident particle. The database composition is shown in Table 2.1. The entries selected involve light ions (neutrons, protons, deuterons, ^3He , and α particles) and photon-induced reactions with energies lower than 200 MeV, *i.e.*, what TALYS can simulate.

Several different definitions of IYR are used to report data in the EXFOR library; therefore the entries were converted to the following definition:

$$IYR_{exp} = \frac{Y_e}{Y_e + Y_g} \quad (2.1)$$

Where Y_e and Y_g are the yields of the excited and the ground state, respectively. It is worthwhile to underline that the definition of Eq. 2.1 is not the same as the one used in Chapter 1 and 3. The spin of the two states is not always specified in the EXFOR entries, making it a non-trivial task to convert the reported IYR to a spin-based definition.

2.3 TALYS models and calculations

TALYS contains six LDMs the user can choose from. Three of them are developed following a phenomenological approach, *i.e.*, they are built using equations based on empirical observations and that agree with the underlying physics. The phenomenological models are the Constant Temperature + Fermi gas model (CTM)[22], the Back-shifted Fermi gas Model (BFM)[23], and the Generalised Superfluid Model (GSM)[24]. The other three models use a microscopic approach where a more detailed mean-field single-particle level scheme and associated pairing is used to tabulate the nuclear level density [21, 25, 26, 27].

The level density $\rho(E_x, J, \Pi)$ is defined as the number of nuclear levels around an excitation energy E_x for a certain spin J and parity Π . In phenomenological models the level density can usually be decomposed as:

$$\rho(E_x, J, \Pi) = P(E_x, J, \Pi)R(E_x, J)\rho_{tot}(E_x) \quad (2.2)$$

Where $P(E_x, J, \Pi)$ is the parity distribution, $\rho_{tot}(E_x)$ is the total LD and $R(E_x, J)$ is the spin distribution [21]. Each of these factors is then calculated differently in the different models.

The spin distribution $R(E_x, J)$ can be altered in TALYS when using the phenomenological models by modifying the spin cut-off parameter σ^2 through a multiplication factor called R_{sc} in Paper I. The effect of modifying R_{sc} (the standard value is 1.0) is to scale the width of the spin distributions of the level density as shown in Figure 2.1.

In Paper I the effect of a variation of R_{sc} between 0.25 and 1.5 is studied.

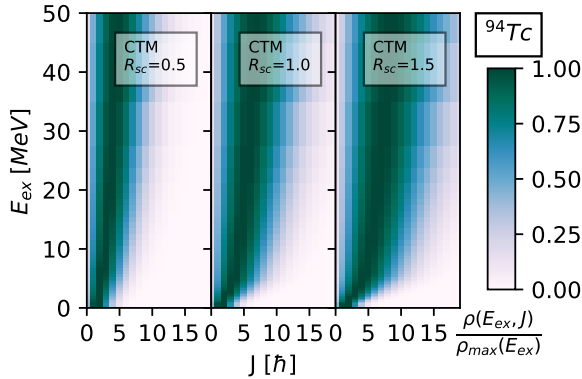


Figure 2.1. Normalized nuclear level density distributions as a function of excitation energy and spin for ^{94}Tc , calculated with TALYS using the CTM level density model. From left to right panel, the plots show how an increasing R_{sc} results in a larger width of the spin distributions [18].

2.4 Comparison between experimental and calculated data

The following analysis procedure focuses on highlighting how TALYS performs for different nuclei. This is why the first step of the analysis process is to calculate, for the i -th EXFOR entry in the database, the weighted mean \bar{X}_i defined as:

$$\bar{X}_i = \frac{\sum_{k=1}^n w_{i,k} (IYR_{exp,i,k} - IYR_{TALYS,i,k})}{\sum_{k=1}^n w_{i,k}} \quad (2.3)$$

Where $IYR_{exp,i,k}$ and $IYR_{TALYS,i,k}$ are the experimental and the corresponding calculated IYRs and $w_{i,k}$ is the squared inverse of the uncertainty of $IYR_{exp,i,k}$ as reported in EXFOR. The sum is performed over all the k measurements in the i -th entry.

Sometimes, an entry can aggregate a very large number of IYRs: 943 entries (83% of the total) are composed by less than 10 measured IYRs, for a total of 2383 individual measured IYR, while the remaining 187 adds up to a total 2976 data points. In other words, 17% of the entries represent 55% of the experimentally measured IYRs. This first step is therefore intended to avoid few specific systems from being over-represented in the results of the analysis.

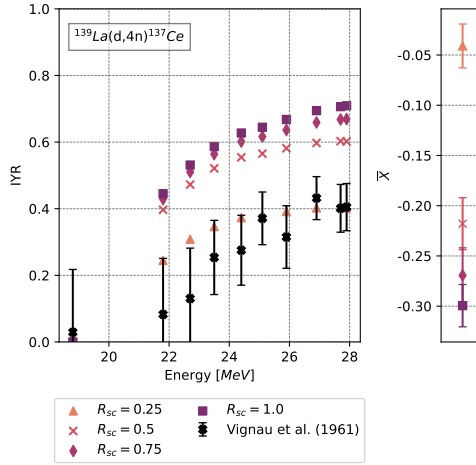


Figure 2.2. On the left, experimental and calculated IYRs for the $^{139}\text{La}(d,4n)^{137}\text{Ce}$ reaction [28]. The calculation results are shown for different R_{sc} values. On the right, the corresponding \bar{X} are plotted. The spin and the parity of the ground and excited states of ^{137}Ce are $J_g = 3/2+$ and $J_e = 11/2-$, respectively [18].

Moreover, the measured IYRs and their uncertainties in one entry are the results of one specific campaign; for this reason their uncertainties are used as weight in 2.3. On the other hand, having comparable uncertainties for every \bar{X}_i would require an intense compilation and evaluation work. Therefore, no

uncertainty is assigned to \bar{X}_i . Figure 2.2 shows this process for one entry [28] and for different values of R_{sc} .

The mean value of \bar{X}_i for all entries and its standard error are calculated as:

$$\begin{aligned} \langle \bar{X} \rangle &= \frac{\sum_{i=1}^m \bar{X}_i}{m} \\ SE &= \sqrt{\frac{\sum_{i=1}^m (\bar{X}_i - \langle \bar{X} \rangle)^2}{m(m-1)}} \end{aligned} \quad (2.4)$$

The value of $\langle \bar{X} \rangle$ can then be used as a figure of merit of the nuclear model code's performances for a specific combination of level density model and R_{sc} and to compare various combinations. This process can also be applied on a smaller part of the data-set, dividing the reactions on the basis of common features to study systematic differences.

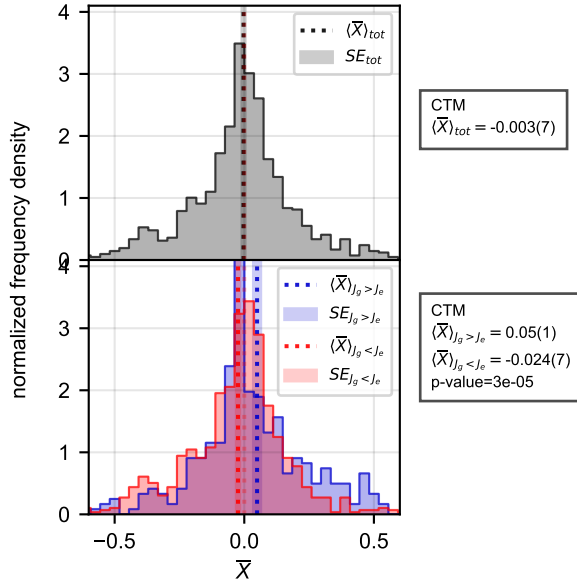


Figure 2.3. Top: \bar{X} distribution for the complete set of data using the CTM model and $R_{sc} = 1.0$. Bottom: \bar{X} distributions dividing the dataset based on the difference between spins of produced nucleus ground and excited states. All three histograms are normalized with respect to the number of entries contained as well as step size [18].

The top plot of Figure 2.3 shows, for CTM and $R_{sc} = 1.0$, the distribution of \bar{X}_i and the value of $\langle \bar{X} \rangle$ for the complete data-set. The same quantities are shown in the bottom plot but collecting nuclei based on whether the ground state spin J_g is smaller (803 entries) or larger (328 entries) than that of the excited state J_e . This plot shows how, on average TALYS, calculations and experimental data are in agreement, while clear difference can be observed

when considering the two sub-sets separately. This trend is also confirmed by the average values, since $\langle \bar{X} \rangle_{J_g < J_e} = -0.024(7)$ while $\langle \bar{X} \rangle_{J_g > J_e} = 0.05(1)$. Moreover, similar results are produced by all six LDMs, as reported in Table 2 of Paper I.

To study the influence of the width of the spin distributions for three phenomenological LDMs, the same process is repeated for several values of R_{sc} to alter the spin cut-off parameter.

2.5 Results and discussion

The analysis shows that the models implemented in TALYS tend to systematically overestimate the yield of the high-spin states. When the ground state of the de-exciting nucleus is the high-spin state, the calculations show that $\langle \bar{X} \rangle_{J_g > J_e} > 0$, *i.e.*, the experimental IYRs are, on average, larger than the calculated ones, according to the definition of Eq. 2.3. The same principle applies if $J_e > J_g$. The over-estimation is compensated by a reduction of the spin cut-off parameter for the macroscopical LDMs, as shown in Figure 2.4, with the convergence of $\langle \bar{X} \rangle_{J_g \leq J_e}$ for $R_{sc} \approx 0.5$. In Paper I this finding is also supported applying the Kolmogorov-Smirnov test, which suggests an optimal value for R_{sc} closer to 0.75. It is also shown how similar behaviours are observed when the incident particles are considered separately.

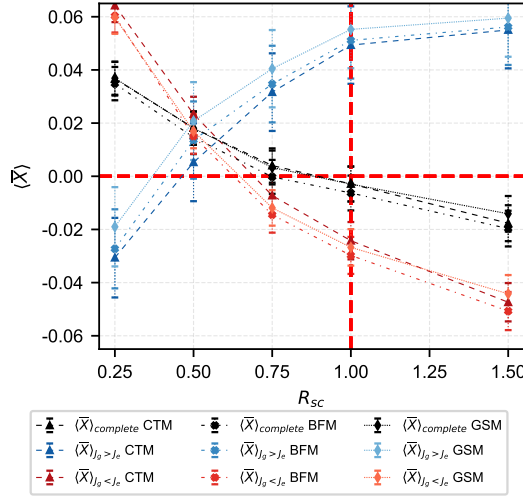


Figure 2.4. Trend of $\langle \bar{X} \rangle$ as a function of R_{sc} for macroscopical LDMs. [18]

A qualitative interpretation of this result is that the effect of reducing R_{sc} on the level densities is to lower the width of the spin distributions, forcing the de-excitation process to converge to lower spin levels. One likely explanation, supported also by other works [29, 30], is that the spin cut-off parameter is

generally overestimated in the modelling. One possible outlook for this work is to extend this investigation to the energy and mass dependence of this effect, as different parametrizations exist for the spin cut-off parameter in the different excitation energy regions.

3. Isomeric yield ratio measurement

3.1 Introduction

Isomeric yield ratio measurements are relevant for a number of reasons, *e.g.*, to test nuclear models, to calculate the angular momentum of fission fragments but may also have technological applications, as the fraction of nuclei in the excited state may affect the decay heat of spent fission fuel [31]. Out of the approximately 800 possible fission products (FP), at least 150 have an observed isomeric state. In a 2021 compilation of yield ratios in fission, Sears *et al.* list 538 experimentally measured IYRs for 62 unique FPs, 39 compound nuclei and 19 different targets [32]. Expanding the analysis to other reactions, at least 5359 experimental IYRs were measured from 1131 reactions (Paper I). More measurements are anyway still needed in order to study the differences between different fissioning systems and nuclei. For this reason, the IYR of 21 FPs of the α -induced fission of ^{232}Th has been measured at 32 MeV at IGISOL in the University of Jyväskylä in Finland, using the JYFLTRAP double Penning trap system.

The energy of the α particles was chosen in order to, at the same time, maximize the cross section of the reaction and to minimize the excitation energy of the fissioning system, *i.e.*, the kinetic energy of the projectile particle. Figure 3.1 shows that 32 MeV roughly corresponds to the beginning of a plateau in the cross section of $^{232}\text{Th}(\alpha, f)$.

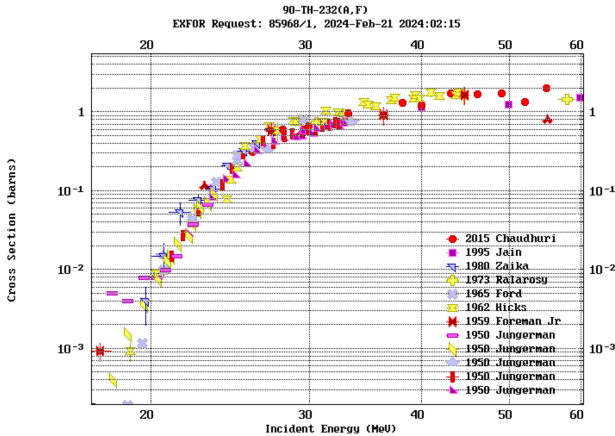


Figure 3.1. Experimental cross sections for $^{232}\text{Th}(\alpha, f)$ with respect to the energy of the projectile α particles.

Nucleus	$T_{\frac{1}{2},g}$ [s]	J_g	E_{exc} [keV]	$T_{\frac{1}{2},e}$ [s]	J_e	Ref.
^{97}Y	3.75(3)	1/2-	667.5(2)	1.17(3)	9/2+	[33]
^{98}Y	0.548(2)	0-	465.70(5)	2.32(8)	7+	[34]
^{100}Y	0.732(5)	1-	$1.4(1) \cdot 10^2$	0.94(3)	4+	[34]
^{99}Nb	15.0(2)	9/2+	365.27(8)	$1.5(1) \cdot 10^2$	1/2-	[33]
^{100}Nb	1.4(2)	1+	$3.1(2) \cdot 10^2$	3.0(1)	5+	[34]
^{102}Nb	4.3(4)	4+	94(7)	1.3(2)	1+	[33]
^{119}Cd	161(1)	1/2+	146.5(1)	132(1)	11/2-	[33]
^{121}Cd	13.5(3)	3/2+	214.9(1)	8.3(8)	11/2-	[33]
^{123}Cd	2.1(3)	3/2+	144(4)	1.8(3)	11/2-	[34]
^{125}Cd	0.68(4)	3/2+	186(4)	0.48(3)	11/2-	[33]
^{119}In	144(6)	9/2+	311.37(3)	$1.08(2) \cdot 10^3$	1/2-	[33]
^{121}In	23.1(6)	9/2+	313.68(7)	233(6)	1/2-	[33]
^{123}In	0.6(3)	9/2+	327.21(4)	47.4(8)	1/2-	[34]
^{125}In	2.36(4)	9/2+	$3.5(1) \cdot 10^2$	12.2(2)	1/2-	[33]
^{127}In	1.086(7)	9/2+	$3.9(2) \cdot 10^2$	3.62(2)	1/2-	[33]
^{129}Sn	134(2)	3/2+	35.15(5)	414(6)	11/2-	[33]
^{132}Sb	167(4)	4+	$1.5(5) \cdot 10^2$	246(3)	8-	[33]
^{133}Te	$7.5(2) \cdot 10^2$	3/2+	334.26(4)	$3.32(2) \cdot 10^3$	11/2-	[33]
^{132}I	$8.26(5) \cdot 10^3$	4+	$1.1(1) \cdot 10^2$	$4.99(5) \cdot 10^3$	8-	[33]
^{134}I	$3.15(1) \cdot 10^3$	4+	316.5(2)	211(2)	8-	[33]
^{136}I	83.4(4)	1-	$2.1(1) \cdot 10^2$	47(1)	6-	[33]

Table 3.1. List of nuclei whose IYR has been measured during the experimental campaign part of this work.

Relevant information for the 21 FPs is provided in Table 3.1, based on the latest assessment from either the NUBASE2020 evaluation [33] or the ENSDF database [34].

Even though ^{232}Th accounts for the 11.7% of the IYRs measured in fission [32], $^{232}\text{Th}(\alpha, f)$ has never been investigated. The results for this system can be compared to measurements for similar fissioning systems to study the effects of the angular momentum added by the incident α particles. Before fissioning, the so-called compound nucleus (CN) formed by ^{232}Th after the capture of the projectile α particle is $^{236}\text{U}^*$. According to both TALYS 2.0 and the reaction simulation code GEF [35], this CN has a 47% chance of releasing two neutrons before splitting. Therefore, the CN mainly formed is $^{234*}\text{U}$ with an estimated excitation energy of approximately 12 MeV. This is expected to be very close to the compound nucleus of $^{233}\text{U}(n_{th}, f)$. The comparison between the angular momenta calculated thanks to the results of these two systems could help answering the question whether the angular momentum is generated before or after scission. Post-scission models are based on the hypothesis that the angular momentum generation takes place after scission, carrying no

memory of the CN. Similar results for different fissioning systems leading to comparable CN would support this hypothesis.

In this chapter, a description of the JYFLTRAP system and the measurement principles are presented (Sec. 3.2), followed by a discussion of the methods used for the analysis of the results (Sec. 3.3). Then the needed corrections are described, to account for the decay in the beamline (Sec.3.4.1) and the possible non-homogeneous efficiency of the position sensitive detector (Sec. 3.4.2). Finally the results are presented for four nuclei (Sec 3.5).

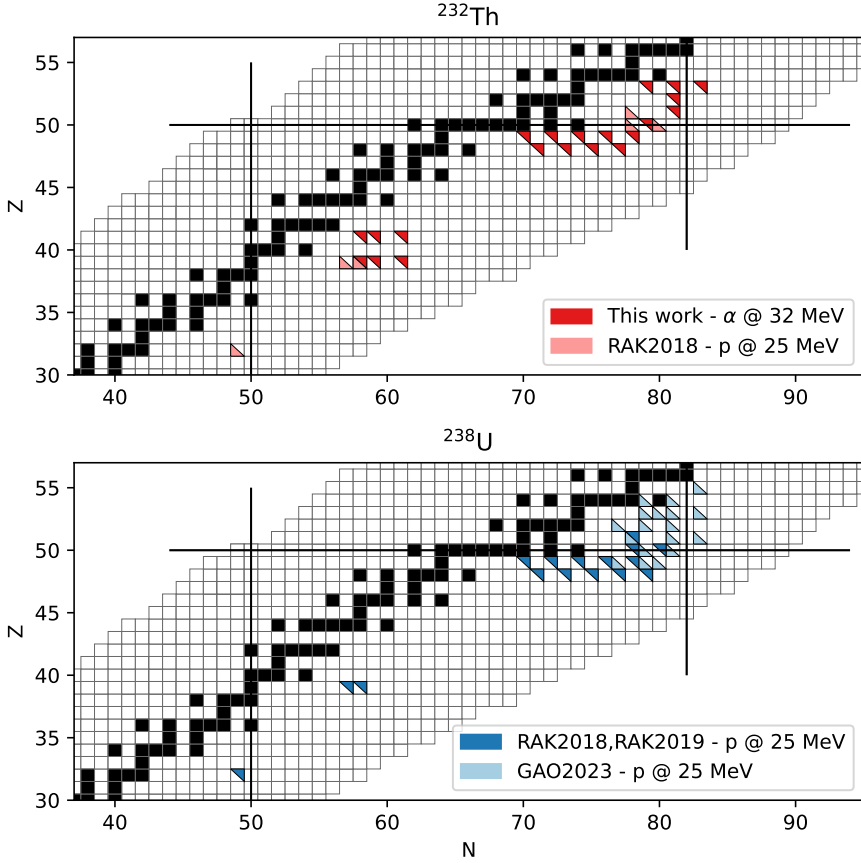


Figure 3.2. Distribution on the nuclear chart of the fission products of ^{238}U ^{232}Th whose IYRs have been measured using the JYFLTRAP double Penning trap. All the IYRs measured by Rakopoulos *et al.* of the FPs of ^{232}Th [13] and the IYRs of $^{96-97}\text{Y}$, ^{128}Sn , ^{130}Sn produced in the fission of ^{238}U [15] have been measured using the side-band cooling technique.

3.2 Experimental setup

The JFYLTRAP system has already been used to measure the IYR of several nuclei (Figure 3.2) produced in the proton induced fission of ^{238}U and ^{232}Th at 25 MeV by Rakopoulos *et al.* and Gao *et al.* [13, 15, 14]. Here the main components will be outlined, focusing on what is more important for the IYR measurement presented in this work.

3.2.1 IGISOL

The Phase-Imaging Ion-Cyclotron-Resonance technique has been applied using the JYFLTRAP double Penning trap at the IGISOL-4 facility in the University of Jyväskylä, shown in Figure 3.3.

Here a beam of α particles accelerated to 32 MeV by the K-130 cyclotron hits a ^{232}Th target. The fission products that escape the target are thermalized by colliding with the He gas, and recombine to form mostly singly charged ions. FFs are then extracted from the target chamber through ion guides, accelerated to 30 kV and mass-separated through a 55° dipole magnet. Here singly charged ions with a particular mass number A are selected with a resolution $R = M/\Delta M \approx 500$. The continuous beam is then slowed down to about 100 eV and bunched using a radiofrequency quadrupole (RFQ) cooler and buncher. The ion bunches are then transported to the trap beamline, where a newly commissioned multi-reflection time-of-flight (MR-TOF) separator is installed before the double Penning trap (JYFLTRAP) and a microchannel plate (MCP) detector. The JYFLTRAP double Penning trap is composed by

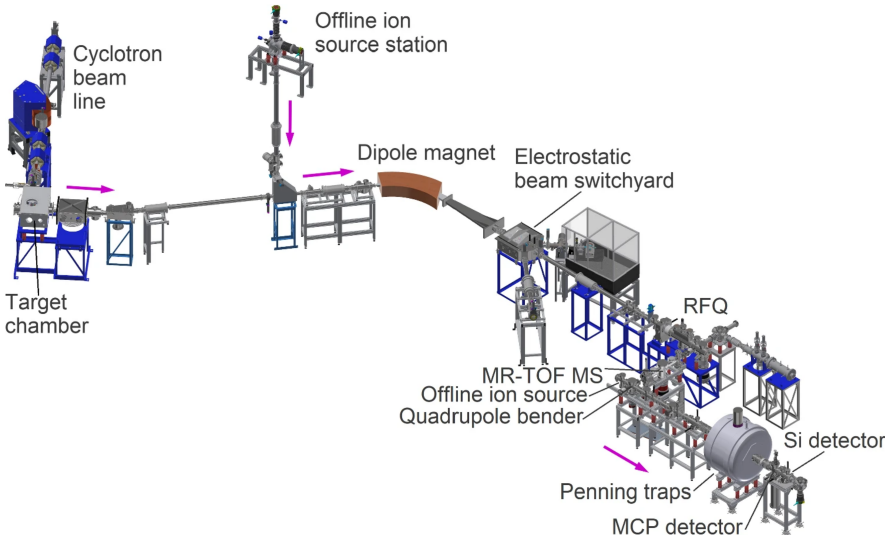


Figure 3.3. Overview of the IGISOL facility layout, outlining the main components and the direction of motion of the ions [36].

two traps installed in a 7T superconducting magnet, providing a field along the beam direction. The first trap is used as a high-resolution mass filter while the second to separate the two isomeric states.

3.2.2 Ions motion in Penning traps

Penning traps are instruments used to confine charged particles through the combination of a homogeneous magnetic field and a quadrupolar electric field. The two fields produce a combination of three eigenmotions: one, called axial motion, takes place along the magnetic field lines with frequency ν_z ; the other two are radial motions, taking place on the plane perpendicular to the field lines. They are called magnetron and modified cyclotron motion and are characterized respectively by their frequencies: the magnetron frequency ν_- , which is independent with respect to the mass of the particles, and the mass-dependant reduced cyclotron frequency ν_+ . Their sum is the cyclotron frequency ν_c , that in an ideal Penning trap is equal to:

$$\nu_+ + \nu_- = \nu_c = \frac{1}{2\pi} \frac{q}{m} B \quad (3.1)$$

where B is the magnetic field, q is the charge of the particle and m is its mass. The magnetron frequency is much larger than the reduced cyclotron frequency; for example, for the measurement of ^{129}Sn , the frequencies are $\nu_+ \approx 833$ KHz, $\nu_- \approx 1.6$ KHz, and $\nu_z \approx 50$ KHz. The ions eigenmotions in Penning traps are manipulated by applying RF fields. When the frequency of the signal matches one of ν_+ and ν_- , the relative eigenmotion is excited. When the RF frequency matches ν_c , the ion motion is converted from one to the other.

3.2.3 Bunch cleaning: side-band cooling technique

The first trap of JYFLTRAP is used for the first purification stage of the bunches through the so-called side-band cooling technique. The purification trap is filled with low-pressure helium gas which slows down the ions through collisions. The bunches entering the first trap are formed by the FFs that have not been stopped by the dipole magnet, *i.e.*, with the same mass number as the nucleus of interest. The goal at this stage is to further clean the unwanted ions off the bunch. Once the bunch is injected in the trap, the magnetron motion is excited through a RF signal with frequency ν_- , increasing the radius of the magnetron motion of all ions. The magnetron motion of a part of the ions is converted into cyclotron motion through an RF signal matching their characteristic ν_c , thus moving at much higher frequency. Higher frequencies correspond to faster rotations and to an higher rate of collisions, *i.e.*, ions moving in a cyclotron motion lose energy significantly faster and their radius decreases

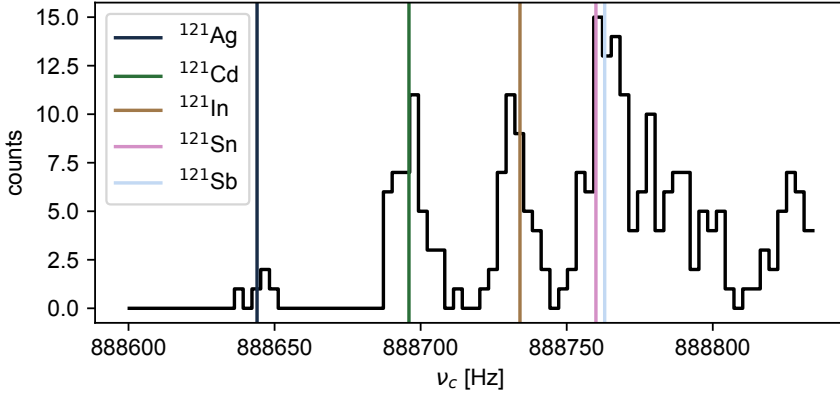


Figure 3.4. Cyclotron frequency spectrum for the measurement of ^{121}Cd . Different peaks correspond to values of ν_c matching the characteristic cyclotron frequency of different ions.

faster over time. Thus, after few milliseconds, the ions whose ν_c corresponds to the RF signal's frequency are focused on the symmetry axis of the trap and the ones whose ν_c does not match the RF will move at a larger radius.

Through the use of a diaphragm in the order of 1-2 millimeters in diameter, only the ions on the symmetry axis of the trap are extracted from the first trap and transported to the second, thus cleaning the bunch. Using this technique, a mass resolving power $M/\Delta M$ of approximately 10^5 can be reached.

The theoretical value of ν_c for a specific q/m can be calculated, while the real one can slightly diverge. To know the correct value for the ions of interest, before each IYR measurement, a scan for several ν_c values is performed. Figure 3.4 shows such a spectrum for the measurement of ^{121}Cd . The peak frequency corresponding to the ion of interest is then used during the actual measurement. In some cases, the cyclotron frequency of different masses lie so close to the used one that a part of the contaminants is extracted from the first trap together with the nucleus of interest. If this happens, ions can be injected again in the first trap and the cleaning process is repeated one more time to suppress contaminants. During this measurement, this process was carried out for $^{119,121,125}\text{Cd}$, $^{119,121}\text{In}$, ^{129}Sn , ^{132}Sb , ^{133}Te , $^{132,134,136}\text{I}$.

Often the contaminants are not completely removed and the remainder are eventually transported to the second trap.

3.2.4 Precision trap: PI-ICR

The dependency of the cyclotron frequency on the mass is used again in the second trap to spatially separate the different nuclei injected. After injection, the reduced cyclotron motion of the ions is excited and, after free revolution

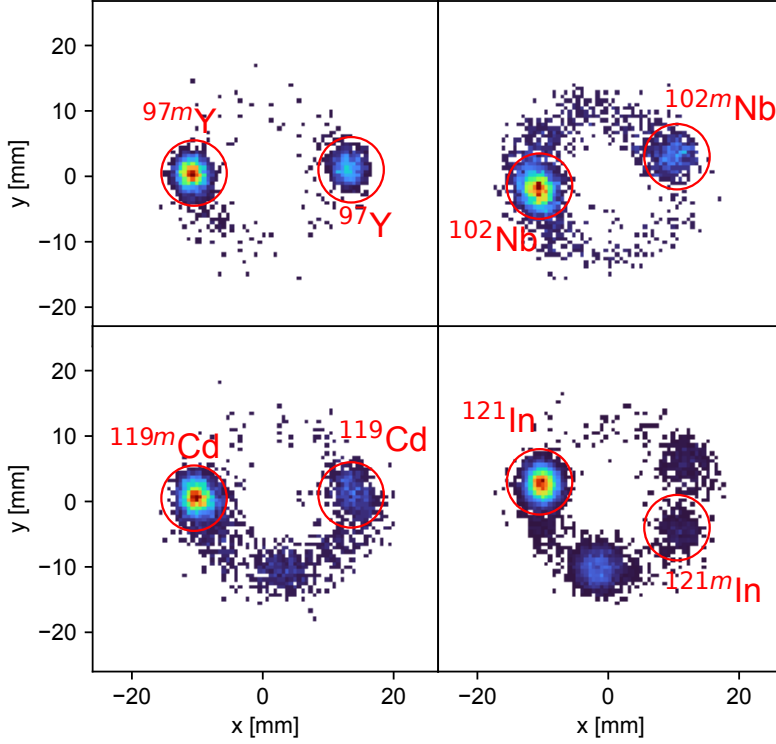


Figure 3.5. PI-ICR image of ^{97}Y (top left), ^{102}Nb (top right), ^{119}Cd (bottom left) and ^{121}In (bottom right).

for a time t , they accumulate a phase given by:

$$2\pi\nu_+t_{acc} = \phi_+ + 2\pi n_+ \quad (3.2)$$

The phase accumulated thus depends on the mass of the nuclei. The ion motion is then slowed down by converting the reduced cyclotron motion into magnetron motion using a quadrupole RF signal and projected onto a position sensitive MCP detector. This technique is called Phase-Imaging Ion-Cyclotron-Resonance (PI-ICR).

Ions with different masses, after a sufficiently long accumulation time, are separated due to the phase difference gained. When projected onto the MCP they generate images like the ones shown in figure 3.5. The four plots give an overview of how the PI-ICR images can look. The ^{102}Nb image shows a very strong tailing effect opposed to ^{97}Y , where a tail is barely visible. The ^{119}Cd and ^{121}In images show the presence of contaminants in the precision trap not

filtered through the side-band cooling technique. The two additional spots in the measurement of ^{119}In are relative to the excited and ground states of ^{121}Cd , producing respectively the low and high intensity spots. On the other hand, the ions producing the third spot in the ^{119}Cd measurement were not fully identified, with candidates being ^{119}Ag or ^{119}In .

3.2.5 PI-ICR for IYR measurements

Ions in the excited and ground states have different energies, masses, and reduced cyclotron frequencies. This results in two spots in a PI-ICR image corresponding to the two states (Figure 3.5). Ideally, each spot corresponds to one nucleus with specific mass present in the second trap; thus these images can be seen as two-dimensional mass spectra.

The correct assignment of the spots to the respective masses is performed before the final data acquisition by varying the accumulation time. Since to larger accumulation time correspond larger separations, the relative position of the spots is studied at different timings to assign them to their species before the actual measurement.

The JYFLTRAP system can also measure the time-of-flight (TOF) of the ions traveling from the purification trap to the MCP detector. These TOF spectra, *e.g.*, the one shown in figure 3.6, usually show a peak around 60 ms, corresponding to the typical time-of-flight of ions. This information can be used to suppress the background by removing the counts with a TOF outside the peak.

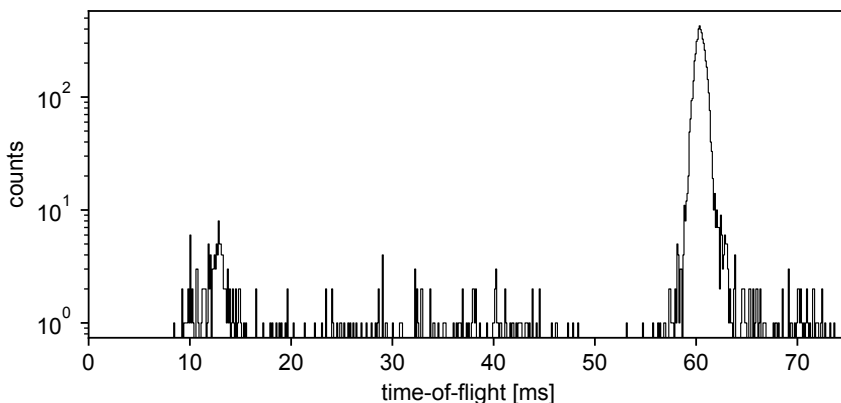


Figure 3.6. Time-of-flight spectrum of ions extraction from purification trap to MCP during the ^{97}Y measurement. Counts outside the peak around 60 ms are considered as background and are filtered out from PI-ICR images.

Finally the measured isomeric yield ratio IYR_{meas} is calculated as:

$$IYR_{\text{meas}} = \frac{C_{hs}}{C_{hs} + C_{ls}} \quad (3.3)$$

Where C_{hs} and C_{ls} are the number of counts in the spot corresponding to, respectively, the high- and low-spin states. At this stage, only the statistical uncertainties associated to C_i are considered, *i.e.*, the square root of the number of counts.

3.3 Identification methods

The ideal shape of spots in PI-ICR images is a 2-dimensional Gaussian, *e.g.*, the one shown by ^{97}Y in Figure 3.5. During this measurement campaign, a relevant number of spots present asymmetrical tails, *i.e.*, decreasingly low counts on one or both sides of the clusters, *e.g.*, the ^{102}Nb case.

The physical explanation of these tails is still unclear, while their relevance in the results of the counting processes has been assessed by applying three methods to identify to which state, if any, the detected ions belong.

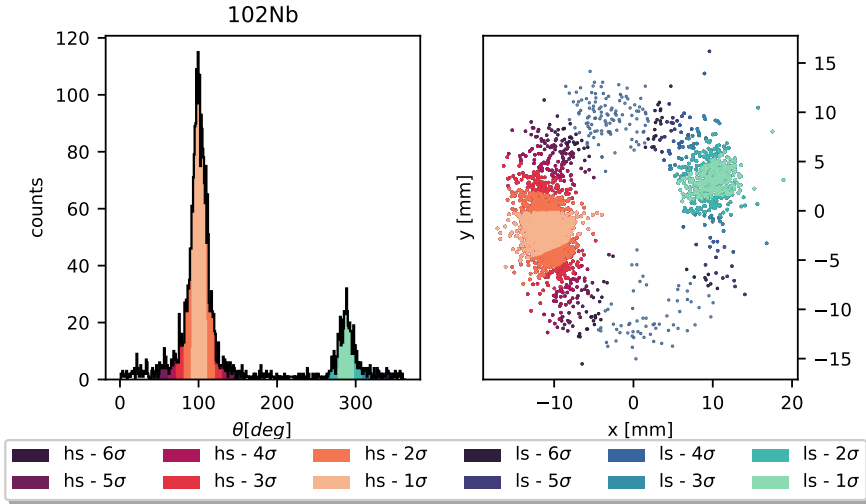


Figure 3.7. On the left, angular position distribution of the ions in the ^{102}Nb measurement, on the right, the corresponding 2-dimensional PI-ICR image. In the legend, 'hs' and 'ls' stand for, respectively, the high-spin and low-spin peaks and spots. The different colors show the integration range for increasingly higher number of σ as range limit.

3.3.1 Angular cut

The first method used starts by calculating the angular distribution of detected ions, *i.e.*, projecting the two-dimensional images on one-dimensional spectra, as shown in Figure 3.7. The peaks corresponding to the isomeric states are then fitted with a Gaussian distribution, which in all cases well describes the main component of the peaks, neglecting the tails where present. Through the fit, the center position θ_p and the standard deviation σ_p of the peaks is calculated; σ_p is then used as a measurement of the size of the spot.

To calculate the number of counts in the spots (C_{hs} and C_{ls}), the numbers of ions detected at angles between $\theta_p - 3\sigma_p$ and $\theta_p + 3\sigma_p$ are summed for the high- and low-spin peaks. Finally eq. 3.3 is used to calculate the IYR. Figure 3.7 shows, for ^{102}Nb , how choosing larger integration windows includes more and more significant parts of the tails, and Figure 3.8 shows the effect on the value of IYR for all isomers. In most cases, 2, 3, and 4σ result in close IYR values. The cases with the largest deviations correspond to the largest tails or where neighbouring spots are present. On this basis, an integration window of 3σ has been chosen to include mainly the Gaussian part of the spots and neglect the tails.

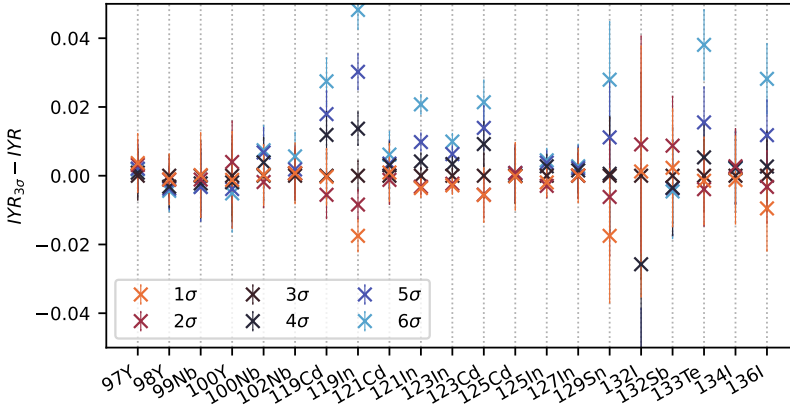


Figure 3.8. IYR values calculated using increasingly larger integration windows normalized with respect to the one calculated at 3σ , *i.e.*, $\text{IYR}_{3\sigma}$, for all the measured isomers.

3.3.2 Angular cut with fitted sigma

The peaks' standard deviation, *i.e.*, spots' size, is observed to depend on the time spent in the precision trap, as shown in Figure 3.9. Even though spots belonging to two isomers are expected to have comparable sizes, few spots have significantly larger sizes with respect to the other spot and the average behaviour. Hence these diverging spots are considered outliers and the de-

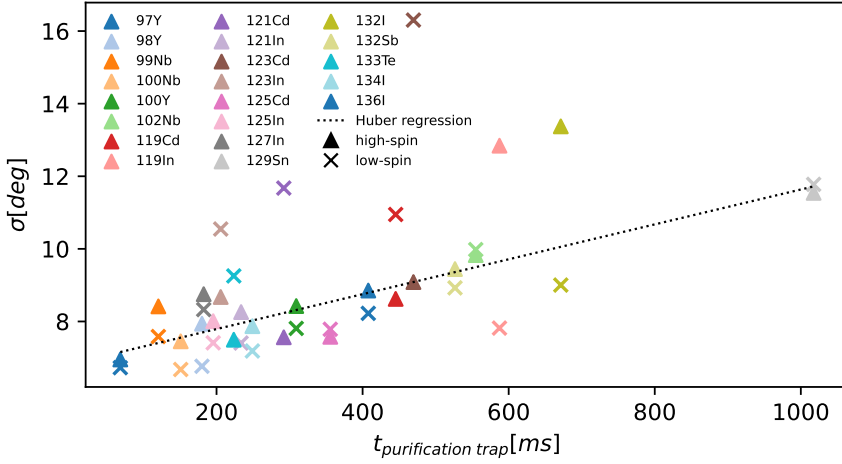


Figure 3.9. Values of σ for all spots calculated through the Gaussian fit of the angular peaks. Additionally the linear curve shows the Huber regression used to fit the $\sigma(t)$ dependency.

pendency $\sigma(t)$ can be fitted through a regression robust to outliers [37]. The resulting function is illustrated by the black dotted curve in Figure 3.9.

This fit is used in the second identification method adopted. It consists of summing the counts inside an integration window, just like the first one. However, the limits of the window are $\theta_p - 3\sigma(t_p)$ and $\theta_p + 3\sigma(t_p)$ where t_p is the time spent in the purification trap and $\sigma(t_p)$ is the theoretical value of the standard deviation calculated through the robust regression. Moreover, the outliers in Figure 3.9 are currently under investigation as their size could be justified as caused by an underlying contamination.

3.3.3 Clustering: OPTICS

Recently, clustering and machine learning methods have been used to analyze more complex PI-ICR images to face different issues, *i.e.*, overlapping spots, non spherical shapes and strong backgrounds [14, 38]. Here the density-based OPTICS (Ordering Points To Identify the Clustering Structure) clustering algorithm is used [39], which identifies, in a dataset, several clusters of data and assigns the points to either one of them or to the background. The idea behind this algorithm is based on the so-called reachability, which is a measure of the distance between a point (in our case a detected ion) and its closest neighbour. The algorithm then sorts the points with similar reachability and that are spatially close, creating the reachability plot, *e.g.*, left plot of Figure 3.10.

Each valley in this kind of plots represents one cluster, while the peaks represent points that may belong to that cluster but that stretch out in space. The

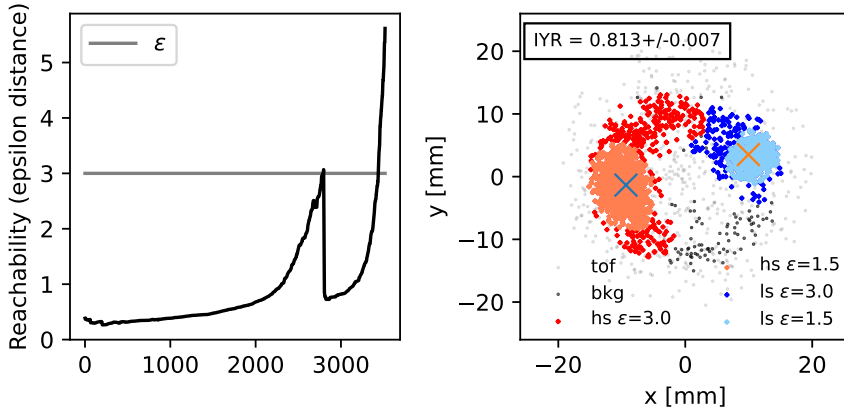


Figure 3.10. Reachability plot (on the left) and result of the clustering algorithm applied to ^{102}Nb PI-ICR image (on the right); 'hs' and 'ls' correspond to the detected ions assigned to respectively high- and low-spin states.

lower the valley is, the more dense the cluster. Therefore, the reachability plot is a description of the overall composition of the dataset and shows the distinct clusters present within it. It can be used to set the maximum distance between two points to consider them as part of the same cluster (ϵ). The parameter ϵ is conventionally set in order to maximize the number of datapoints in the lowest of the two peaks. The motivation for this convention is to consistently include as much of the tails in the PI-ICR images as possible. Figure 3.10 shows, as an example, that in ^{102}Nb analysis $\epsilon = 3$, *i.e.*, just below the peak value of the reachability for the denser spot. With a larger value, the algorithm would consider only one cluster. The effect of a smaller value is also shown in 3.10, where the ions considered as corresponding to the two spots for $\epsilon = 1.5$ are shown in lighter colors. In this case, the corresponding IYR would be equal to 0.847(6).

3.3.4 Comparison between identification methods

The described methods have been chosen to compare three different ways of dealing with tails: a very strict approach (angular cut with $\sigma(t)$) to cut them as much as possible, a less stringent one (angular cut with σ_p) and one method which consistently includes them (clustering). Figure 3.11 shows the results for the same four nuclei shown in Figure 3.5. The plot shows that the three methods yield very similar results for all the considered nuclei. In the case of ^{119}Cd , however, the IYR values spread more with respect to the other nuclei while the uncertainty ranges still overlap. Moreover, the method which scores consistently closer to the average value is the angular cut with fitted sigma.

The angular cut with fitted sigma is eventually selected to calculate the IYR and its statistical uncertainty. To account for the contribution of the tails, the uncertainty is enlarged when the results of the three methods do not match: if the standard deviation of the IYRs calculated using all three methods is larger than the statistical uncertainty, the uncertainty is set to be equal to the standard deviation itself.

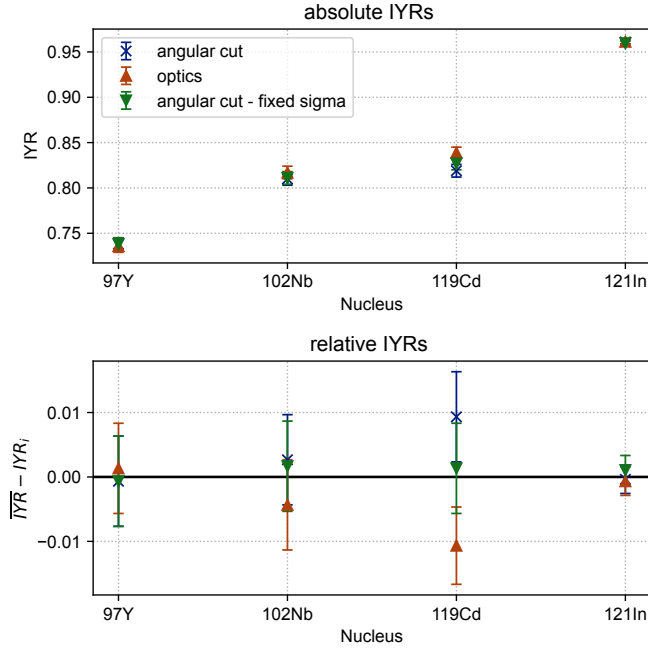


Figure 3.11. IYRs calculated through angular cut, optics and angular cut with fitted sigma methods for ^{97}Y , ^{102}Nb , ^{119}Cd and ^{121}In . IYRs are shown both in absolute (top) and relative (bottom) scale with respect to the average of the three IYRs for the specific nucleus.

3.4 Corrections

The analysis methods discussed so far are used to calculate the ratio between the yields of isomeric states in the precision Penning trap. In order to calculate the ratio of the fission products, it is necessary to account for the decay of the nuclei from production until they arrive at the MCP and the efficiency of the position sensitive detectors.

3.4.1 Decay correction

When the half-lives of the nucleus under analysis and its precursors are on the order of few seconds or less, they are comparable to the transport time from the fission chamber to the MCP, in the order of 0.5-1s. In such cases, the decay and feeding effects from the precursors can be relevant and significantly affect the measured IYR.

For this reason, a decay correction is applied where the transport process is represented by four steps, one for each time-relevant stage of the ion transport, *i.e.*, gas-cell, RFQ cooler-buncher, purification and precision trap. The idea is to assume an initial value for the IYR in the gas-cell, simulate the transport process and compare the result to the measured value, changing the initial IYR until the simulated and experimentally measured IYRs converge.

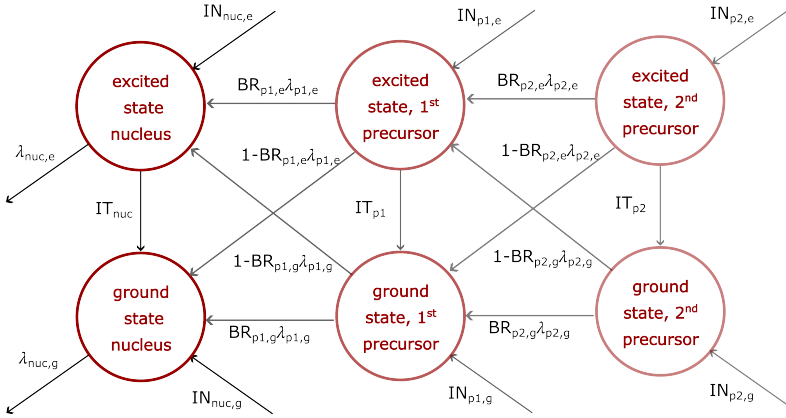


Figure 3.12. Overview of the decay correction schema independently of the nucleus and the stage considered.

On a general level, each time period is divided into 1 ms steps and for each of them a balance equation is calculated for the excited and ground state of the nucleus of interest, and for the first and second precursors. In each time interval the a state can decay and be fed as summarized in the following.

- Decay:
 - A state can β -decay to the daughter nucleus with a characteristic half life λ_i . The decay can either be to the excited or the ground state, with a branching ratio respectively of BR_i and $1-BR_i$;
 - Excited states can decay to the ground state through internal transition, with a probability equal to IT_i ;
- Feeding:
 - A state can be fed by one of the two previous events;

- A state can be fed by an "external source" IN_i , *i.e.*, fission events in the gas-cell and ions coming from the gas-cell when considering the RFQ cooler-buncher.

Figure 3.12 is a representation of the set of transitions that may happen and that are calculated for each time interval. This may simplify in some cases as the precursors may not have a long-lived excited state and some of these transitions may have probabilities equal to zero.

Each of the four stages differs in the external source term, which species are present and time length as presented in the following.

1. Gas-cell: the external source terms here are the fission events feeding the i -th state at a rate proportional to the fission yield (FY_i) and the respective IYR_i . This is where the trial IYR is set for the convergence calculation. It is estimated that, on average, it takes 100 ± 10 ms to extract fission fragments from the gas-cell where they are produced. Since it is not possible to measure this value, this time is assumed to be the same for all measurements
2. RFQ cooler-buncher: at this stage, ions extracted from the gas-cell are trapped and bunched until the bunches are released to the first trap. Therefore the external source term here is the result of the previous stage. The length of this and the next two stages is set during the measurement, therefore it is known, and it can range from few tens of ms to hundreds of ms, depending on the half-life of the nuclei of interest.
3. Purification trap: Once the bunch is injected in the purification trap it is isolated from the beamline. Therefore at this stage, the trap contains the nuclei of interest and its precursors, while there is no external source. The nuclei usually spend 100-300 ms in the purification trap.
4. Precision trap: the same condition as the first trap holds for the precision trap. Moreover here the precursors are, in principle, not present. The calculations do not take into account the presence of possible contamination. The length of this final step depends on the time required to spatially separate the nuclei in the trap, and can range from few hundreds ms to almost 1s, *e.g.*, in the case of ^{129}Sn .

The input parameters of these calculations are half-lives (λ_i), fission yields (FY_i) and branching ratios (BR_i). The λ_i are taken either from the Nubase2020 evaluation [33] or ENSDF database [34] (Tab 2.1). FY_i and IYR_i are calculated simulating the 32 MeV alpha-particle induced fission of ^{232}Th using GEF [35]. Finally, BR_i are estimated using the ENSDF decay schemes.

To calculate the uncertainty associated to the corrected IYR value, the calculation is repeated 10^6 times sampling the values of the parameters at each iteration. To include the statistical uncertainty, the value of the measured IYR is resampled as well within the statistical uncertainty.

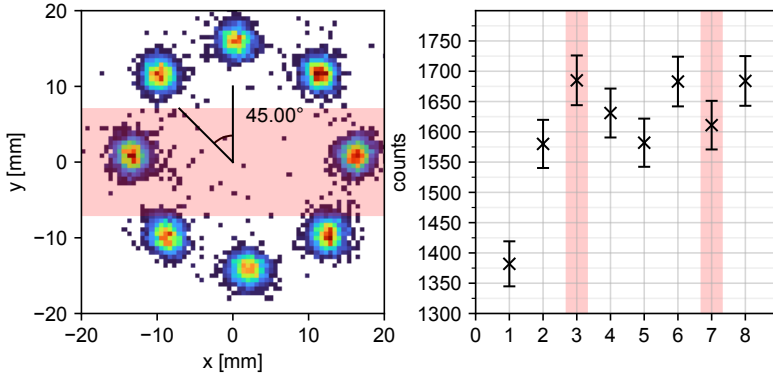


Figure 3.13. PI-ICR image of sensitivity measurement (left) and correspondent number of counts for each spot (right). Spots are numbered counterclockwise in ascending order, where zero corresponds to the spot close to zero degrees.

3.4.2 MCP efficiency correction

A non-homogeneous sensitivity of MCP detectors can significantly affect IYR measurements and recent studies have shown that the IYR measurement may change depending on the position of the spots [40]. To investigate this effect, an initial characterization of the MCP was performed by producing several spots in relevant positions for the analysis, by progressively changing the accumulation time using a ^{133}Cs internal source, in order to reproduce the experimental conditions of the actual measurements. Figure 3.13 shows the sensitivity measurement and the number of counts for each spot as a function of the angle.

The plot shows a slightly non-homogeneous sensitivity for the angles between 45° and 315° and a severe decrease at 0° , corresponding to the top of the detector.

In order to mitigate this effect, the measurements have always been performed in the same region, corresponding to the equatorial range around 90° and 270° . Moreover, for each nucleus, two separate measurements have been performed. The two measurements are called "standard" and "mirrored", based on the position of the high-spin state, positioned respectively at 90° and 270° for the two configurations, and the other way round for the low-spin state.

Based on the results obtained (Figure 3.14 and Table 3.2), and preliminary analysis on the rest of the nuclei included in the experimental campaign, there is no significant difference between the two configurations. Therefore, the two measurements are combined and used to calculate the final experimental IYR.

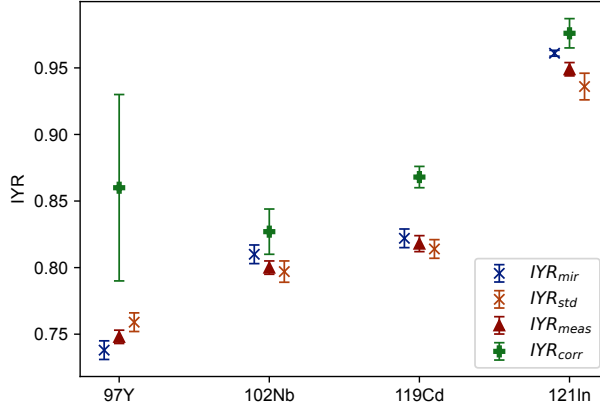


Figure 3.14. The blue and orange markers show the IYR of ^{97}Y , ^{102}Nb , ^{119}Cd and ^{121}In measured in, respectively, standard and mirrored configurations. The red markers shows the combination of the two measurements and the green markers show the combined IYRs values after the decay correction.

3.4.3 Effect of the corrections

Figure 3.14 and Table 3.2 show the effect of both the decay and the MCP efficiency corrections for the four nuclei considered so far. In the plot, IYR_{std} and IYR_{mir} are the two ratio values calculated as presented in Section 3.3 for the standard and mirrored configurations. In the same plot, IYR_{meas} and IYR_{corr} represent, respectively, the ratio obtained combining the counts for the two configurations and the one calculated after applying the decay correction on it.

The data show that the MCP efficiency can be considered homogeneous and not affecting the final results. On the other hand, the decay correction can be significant and can also introduce a general increase in the uncertainty of the final IYR. This is given by the combination of the different uncertainties of the fission yields, half-lives and branching ratios for the nucleus of interest and the precursors.

3.5 Results and discussion

The results of the analysis described so far are shown in Figure 3.15 for ^{97}Y , ^{102}Nb , ^{119}Cd and ^{121}In . The plot also shows literature data of the yield ratios measured for other fissioning systems [13, 14, 15, 41, 42] as reported by Sears *et al.* [32] as a reference. It is found that the IYRs of ^{97}Y and ^{102}Nb are significantly larger than the ones measured for other fissioning systems, except for, in part, $^{232}\text{Th}(p,f)$ at 25 MeV. On the other hand, at higher masses and closer to the symmetric fission region, ^{119}Cd and ^{121}In show similar results

with respect to the products of $^{238}\text{U}(\text{p},\text{f})$ at 24 and 25 MeV. Therefore, Figure 3.15 shows two different behaviours in the two mass regions considered.

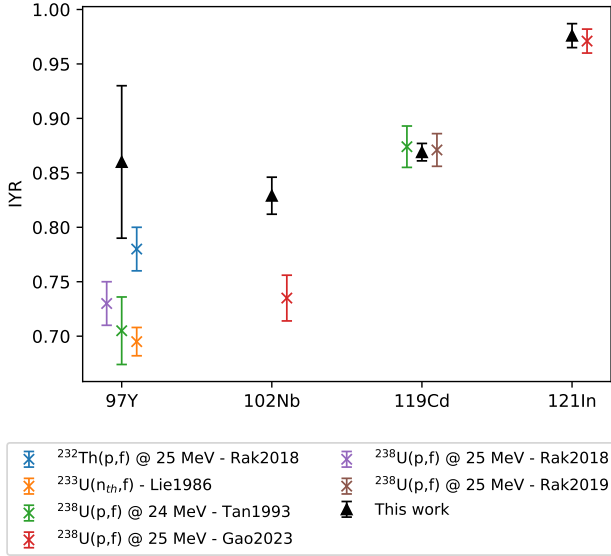


Figure 3.15. Values of IYR after decay correction for ^{97}Y , ^{102}Nb , ^{119}Cd and ^{121}In compared to literature data for the same fission products.

nucleus	IYR_{std}	IYR_{mir}	IYR_{meas}	IYR_{corr}
^{97}Y	0.759(7)	0.738(7)	0.748(5)	0.86(7)
^{102}Nb	0.797(8)	0.810(7)	0.800(5)	0.83(2)
^{119}Cd	0.814(7)	0.822(7)	0.818(6)	0.868(8)
^{121}In	0.94(1)	0.961(2)	0.949(5)	0.98(1)

Table 3.2. Measured (*m*), corrected (*c*) and final values of IYRs for ^{97}Y , ^{102}Nb , ^{119}Cd and ^{121}In for standard (*std*) and mirrored (*mir*) configurations.

A larger IYR may correspond to an increased average angular momentum of the de-exciting fission fragment, as the transitions to energy levels with larger spins seems to be favoured. If this is true, the preliminary data presented in Figure 3.15 could show that the the 32 MeV alpha-particle induced fission of ^{232}Th might produce FFs with comparable or higher angular momenta then those produced as a result of the proton induced fission of ^{238}U and calculated by Gao *et al.* [17].

This is a trend that will be investigated once the analysis will be extended to the rest of the dataset.

4. Conclusions and future outlook

A deeper understanding of angular momentum generation is an important step to a conclusive theory of fission dynamics. Both parts of this work, stronger nuclear models and reliable experimental data, are necessary elements of more solid angular momentum estimations.

The study regarding level density models is a piece of a more general and continuous effort towards better modeling of nuclear reactions. The availability of a growing number of accurate data facilitates comprehensive works where codes are tested with respect to various systems and, at the same time, systematic effects can be studied. Making use of these data, a bias was found in the models with respect to the spin of the de-exciting nuclei and the effect of the spin distributions was studied. The results of this work showed that an improvement of the parametrization of the spin cut-off parameter, currently based on the rigid body moment of inertia, could improve the calculations of the isomeric yield ratio. Súdár *et al.* showed that moment of inertia calculated under the assumption of a rotating rigid body is often overestimated. They also showed that the ratio between effective and rigid body moment of inertia depends on the evenness and oddness of atomic and neutron numbers and on the mass number. Therefore, this work could be expanded by looking for the same dependency.

Compared to past experimental campaigns, the isomeric yield ratio measurements presented new challenges which are still being addressed. The initial results are promising, although the analysis still needs to be expanded to the remaining nuclei. The values and the uncertainties are in line with the ones from past experiments.

Moreover, during the second year of my PhD, I joined the Fragments Separator Ion Catcher (FRS-IC) collaboration [43], spending four months at the GSI facility in Darmstadt (Germany), working at the operation of a cryogenic stopping cell. The goal of this collaboration is to use the high-resolution mass spectra of the multi-reflection time-of-flight mass spectrometer (MR-TOF MS) to measure the isomeric yield ratios of fission fragments produced in the spontaneous fission of ^{252}Cf and ^{244}Cm . Mass spectra have also been collected using a recently commissioned MR-TOF MS at IGISOL, where several isomers could be identified, like, *e.g.*, ^{96}Y and ^{97}Y . The MR-TOF MS, to the best of my knowledge, has not been used yet to measure isomeric yield ratios, therefore these mass spectra require the development of new analysis procedures that will be faced in the development of this work.

Once the analysis of isomeric yield ratios will be complete, the new ratios will be used to calculate the angular momentum of the fission fragments. To do so, the starting point will be the advances recently achieved in this method by Gao *et al.* [17].

To further develop this method, several ratios may be used in parallel to extract the angular momentum of more than one fission fragment. The idea is to develop a model to vary, for a certain atomic number, the energy and angular momentum of all the fission fragments and assesses the impact on the calculated ratios of the nuclei with the same proton number, until all of them match the experimental values within uncertainties. This is facilitated by the composition of the dataset, where several series of nuclei with the same atomic number are present, *i.e.* Y, Nb, Cd, In, I. This new method could increase the computational time but may lead to an improved model for the angular momentum calculation.

Acknowledgement

This project has received funding from the Euratom research and training programme 2014-2018 under grant agreement No847594 (ARIEL) and is supported by the Swedish Research Council (Ref. No. 2020-04238).

References

- [1] L. Meitner and O. R. Frisch, “Disintegration of Uranium by Neutrons: A New Type of Nuclear Reaction,” *Nature*, vol. 143, no. 3615, pp. 239–240, 1939.
- [2] N. Bohr and J. A. Wheeler, “The mechanism of nuclear fission,” *Phys. Rev.*, vol. 56, pp. 426–450, Sep 1939.
- [3] G. Gamow, “Mass Defect Curve and Nuclear Constitution,” *Proceedings of the Royal Society of London Series A*, vol. 126, pp. 632–644, Mar. 1930.
- [4] J. B. Wilhelmy, E. Cheifetz, R. C. Jared, S. G. Thompson, H. R. Bowman, and J. O. Rasmussen, “Angular Momentum of Primary Products Formed in the Spontaneous Fission of Cf 252,” *Physical Review C*, vol. 5, pp. 2041–2060, June 1972.
- [5] A. N. Andreyev, K. Nishio, and K.-H. Schmidt, “Nuclear fission: A review of experimental advances and phenomenology,” *Reports on Progress in Physics*, vol. 81, p. 016301, Jan. 2018.
- [6] J. N. Wilson, D. Thisse, M. Lebois, N. Jovančević, D. Gjestvang, R. Canavan, M. Rudigier, D. Étasse, R.-B. Gerst, L. Gaudefroy, E. Adamska, P. Adsley, A. Algora, M. Babo, K. Belvedere, J. Benito, G. Benzoni, A. Blazhev, A. Boso, S. Bottoni, M. Bunce, R. Chakma, N. Cieplicka-Oryńczak, S. Courtin, M. L. Cortés, P. Davies, C. Delafosse, M. Fallot, B. Fornal, L. Fraile, A. Gottardo, V. Guadilla, G. Häfner, K. Hauschild, M. Heine, C. Henrich, I. Homm, F. Ibrahim, Ł. W. Iskra, P. Ivanov, S. Jazrawi, A. Korgul, P. Koseoglou, T. Kröll, T. Kurtukian-Nieto, L. Le Meur, S. Leoni, J. Ljungvall, A. Lopez-Martens, R. Lozeva, I. Matea, K. Miernik, J. Nemer, S. Oberstedt, W. Paulsen, M. Piersa, Y. Popovitch, C. Porzio, L. Qi, D. Ralet, P. H. Regan, K. Rezyrkina, V. Sánchez-Tembleque, S. Siem, C. Schmitt, P.-A. Söderström, C. Sürder, G. Tocabens, V. Vedia, D. Verney, N. Warr, B. Wasilewska, J. Wiederhold, M. Yavahchova, F. Zeiser, and S. Ziliani, “Angular momentum generation in nuclear fission,” *Nature*, vol. 590, pp. 566–570, Feb. 2021.
- [7] J. Randrup and R. Vogt, “Generation of Fragment Angular Momentum in Fission,” *Physical Review Letters*, vol. 127, p. 062502, Aug. 2021.
- [8] A. Bulgac, “The angular correlation between the fission fragment intrinsic spins,” *Physical Review C*, vol. 106, p. 014624, July 2022.
- [9] R. Vogt and J. Randrup, “Angular momentum effects in fission,” *Physical Review C*, vol. 103, p. 014610, Jan. 2021.
- [10] P. Marević, N. Schunck, J. Randrup, and R. Vogt, “Angular momentum of fission fragments from microscopic theory,” *Physical Review C*, vol. 104, p. L021601, Aug. 2021.
- [11] P. Walker and G. Dracoulis, “Energy traps in atomic nuclei,” *Nature*, vol. 399, no. 6731, pp. 35–40, 1999.
- [12] J. R. Huizenga and R. Vandenbosch, “Interpretation of Isomeric Cross-Section Ratios for (n, γ) and (γ ,n) Reactions,” *Physical Review*, vol. 120, pp. 1305–1312, Nov. 1960.

- [13] V. Rakopoulos, M. Lantz, A. Solders, A. Al-Adili, A. Mattera, L. Canete, T. Eronen, D. Gorelov, A. Jokinen, A. Kankainen, V. S. Kolhinen, I. D. Moore, D. A. Nesterenko, H. Penttilä, I. Pohjalainen, S. Rinta-Antila, V. Simutkin, M. Vilén, A. Voss, and S. Pomp, “First isomeric yield ratio measurements by direct ion counting and implications for the angular momentum of the primary fission fragments,” *Physical Review C*, vol. 98, p. 024612, Aug. 2018.
- [14] Z. Gao, A. Solders, A. Al-Adili, S. Cannarozzo, M. Lantz, S. Pomp, O. Beliuskina, T. Eronen, S. Geldhof, A. Kankainen, I. D. Moore, D. Nesterenko, and H. Penttilä, “Isomeric yield ratios in proton-induced fission of ^{238}U ,” *Phys. Rev. C*, vol. 108, p. 054613, Nov 2023.
- [15] V. Rakopoulos, M. Lantz, S. Pomp, A. Solders, A. Al-Adili, L. Canete, T. Eronen, A. Jokinen, A. Kankainen, A. Mattera, I. Moore, D. Nesterenko, M. Reponen, S. Rinta-Antila, A. De Roubin, M. Vilén, M. Österlund, and H. Penttilä, “Isomeric fission yield ratios for odd-mass cd and in isotopes using the phase-imaging ion-cyclotron-resonance technique,” *Physical Review C*, vol. 99, no. 1, 2019.
- [16] A. Al-Adili, V. Rakopoulos, and A. Solders, “Extraction of angular momenta from isomeric yield ratios: Employing talys to de-excite primary fission fragments,” *European Physical Journal A*, vol. 55, no. 4, 2019.
- [17] Z. Gao, *Isomeric yield ratios in nuclear fission*. PhD thesis, Uppsala, 2023.
- [18] S. Cannarozzo, S. Pomp, A. Solders, A. Al-Adili, A. Göök, and A. Koning, “Global comparison between experimentally measured isomeric yield ratios and nuclear model calculations,” *European Physical Journal A*, vol. 59, no. 12, 2023.
- [19] “EXFOR: Experimental Nuclear Reaction Data.”
<https://www-nds.iaea.org/exfor/>.
- [20] A. J. Koning, S. Hilaire, and S. Goriely, “TALYS-2.0: Simulation of nuclear reactions.” <https://www-nds.iaea.org/exfor/>, 2023.
- [21] A. Koning, S. Hilaire, and S. Goriely, “Talys: modeling of nuclear reactions,” *European Physical Journal A*, vol. 59, no. 6, 2023.
- [22] A. Gilbert and A. G. W. Cameron, “A composite nuclear-level density formula with shell corrections,” *Canadian Journal of Physics*, vol. 43, no. 8, pp. 1446–1496, 1965.
- [23] W. Dilg, W. Schantl, H. Vonach, and M. Uhl, “Level density parameters for the back-shifted fermi gas model in the mass range $40 < A < 250$,” *Nuclear Physics A*, vol. 217, no. 2, pp. 269–298, 1973.
- [24] A. V. Ignatyuk, K. K. Istekov, and G. N. Smirenkin, “Role of collective effects in the systematics of nuclear level densities,” *Sov. J. Nucl. Phys. (Engl. Transl.)*; (*United States*), vol. 29, 4 1979.
- [25] P. Demetriou and S. Goriely, “Microscopic nuclear level densities for practical applications,” *Nuclear Physics A*, vol. 695, no. 1, pp. 95–108, 2001.
- [26] S. Goriely, S. Hilaire, and A. J. Koning, “Improved microscopic nuclear level densities within the Hartree-Fock-Bogoliubov plus combinatorial method,” *Phys. Rev. C*, vol. 78, p. 064307, Dec 2008.
- [27] S. Hilaire, M. Girod, S. Goriely, and A. J. Koning, “Temperature-dependent combinatorial level densities with the DIM Gogny force,” *Phys. Rev. C*, vol. 86, p. 064317, Dec 2012.

- [28] H. Vignau and S. J. Nassiff, “Yield Ratios of the Isomeric Pair $\text{Ce}^{137m}/\text{Ce}^{137}$ Formed by $\text{La}^{139}(\text{d},\text{n})\text{Ce}^{137}$ Reaction,” *Nuclear Physics*, vol. 26, p. 108, 1961.
- [29] L.-L. Liu, Y.-Y. Liu, X.-L. Huang, J.-M. Wang, Y.-J. Chen, N.-C. Shu, and Z.-G. Ge, “Influence of the spin cut-off parameter on the isomeric cross-section ratio of the $(n, 2n)$ reaction within the huiZenga-vandenbosch method,” *Phys. Rev. C*, vol. 109, p. 014603, Jan 2024.
- [30] S. Sudár and S. Qaim, “Mass number and excitation energy dependence of the $\theta_{eff}/\theta_{rig}$ parameter of the spin cut-off factor in the formation of an isomeric pair,” *Nuclear Physics A*, vol. 979, pp. 113–142, 2018.
- [31] A. A. Sonzogni, E. A. McCutchan, T. D. Johnson, and P. Dimitriou, “Effects of fission yield data in the calculation of antineutrino spectra for $^{235}\text{U}(n, \text{fission})$ at thermal and fast neutron energies,” *Phys. Rev. Lett.*, vol. 116, p. 132502, Apr 2016.
- [32] C. Sears, A. Mattera, E. McCutchan, A. Sonzogni, D. Brown, and D. Potemkin, “Compilation and evaluation of isomeric fission yield ratios,” *Nuclear Data Sheets*, vol. 173, pp. 118–143, 2021.
- [33] F. Kondev, M. Wang, W. Huang, S. Naimi, and G. Audi, “The NUBASE2020 evaluation of nuclear physics properties,” *Chinese Physics C*, vol. 45, p. 030001, mar 2021.
- [34] National Nuclear Data Center, “From ENSDF database as of 02/21, 2024. version available at <http://www.nndc.bnl.gov/ensarchivals/>,” 2024. <http://www.nndc.bnl.gov/ensarchivals/> [Accessed: (21/02/24)].
- [35] K.-H. Schmidt, B. Jurado, C. Amouroux, and C. Schmitt, “General description of fission observables: Gef model code,” *Nuclear Data Sheets*, vol. 131, pp. 107–221, 2016. Special Issue on Nuclear Reaction Data.
- [36] D. A. Nesterenko, T. Eronen, Z. Ge, A. Kankainen, and M. Vilen, “Study of radial motion phase advance during motion excitations in a Penning trap and accuracy of JYFLTRAP mass spectrometer,” *The European Physical Journal A*, vol. 57, p. 302, Nov. 2021.
- [37] P. J. Huber, “Robust Estimation of a Location Parameter,” *The Annals of Mathematical Statistics*, vol. 35, no. 1, pp. 73 – 101, 1964.
- [38] C. Weber, D. Ray, A. Valverde, J. Clark, and K. Sharma, “Gaussian mixture model clustering algorithms for the analysis of high-precision mass measurements,” *Nuclear Instruments and Methods in Physics Research, Section A: Accelerators, Spectrometers, Detectors and Associated Equipment*, vol. 1027, 2022.
- [39] M. Ankerst, M. M. Breunig, H.-P. Kriegel, and J. Sander, “Optics: Ordering points to identify the clustering structure,” in *Proceedings of the 1999 ACM SIGMOD International Conference on Management of Data*, SIGMOD ’99, (New York, NY, USA), pp. 49–60, Association for Computing Machinery, 1999.
- [40] Z. Gao, A. Solders, A. Al-Adili, O. Beliuskina, T. Eronen, A. Kankainen, M. Lantz, I. Moore, D. Nesterenko, H. Penttilä, S. Pompi, and H. Sjöstrand, “Applying machine learning methods for the analysis of two-dimensional mass spectra,” *European Physical Journal A*, vol. 59, no. 7, 2023.
- [41] C. Lietz, H. O. Denschlag, W. Ditz, U. Guttler, B. Sohnius, P. Stumpf, and H. Faust, “Isomeric ratios and distribution of angular momentum in the reaction $^{233}\text{U}(n_{th}, f)$ at various kinetic energies of the fragments,” Progress Report

- 272U,(5), 1986. Report from CEC-Countries and CEC to NEANDC.
- [42] M. Tanikawa, H. Kudo, H. Sunaoshi, M. Wada, T. Shinozuka, and M. Fujioka, "Isomeric yield ratios of fission products in the system of 24 mev proton-induced fission of ^{238}U ," *Zeitschrift für Physik A Hadrons and Nuclei*, vol. 347, no. 1, pp. 53–62, 1993.
- [43] T. Dickel, W. Plaß, A. Becker, U. Czok, H. Geissel, E. Haettner, C. Jesch, W. Kinsel, M. Petrick, C. Scheidenberger, A. Simon, and M. Yavor, "A high-performance multiple-reflection time-of-flight mass spectrometer and isobar separator for the research with exotic nuclei," *Nuclear Instruments and Methods in Physics Research Section A: Accelerators, Spectrometers, Detectors and Associated Equipment*, vol. 777, pp. 172–188, 2015.